THE JOURNAL OF PHYSICAL CHEMISTRY C
A JOURNAL OF THE AMERICAN CHEMICAL SOCIETY

pubs.acs.org/JPCC

Article

Electric Field Manipulation for Improved Rates of Photocatalysis by Mesoporous TiO_2

Qilong Huang and Edmund G. Seebauer*

Cite This: *J. Phys. Chem. C* 2022, 126, 1376−1388

Read Online

ACCESS | Metrics & More | Article Recommendations | Supporting Information

ABSTRACT: This work demonstrates a concept for improving rates of photocatalysis by mesoporous thin films of semiconducting oxide nanoparticles through manipulating the built-in electric field near the nominal free surface. The reaction rate increases via combinations of donor concentration and surface potential that yield wide space charge widths and correspondingly large regions encompassed by the built-in field. The field draws minority carriers generated deep within the film toward the nominal surface where the chemical reactant is most concentrated. In the photo-oxidation of aqueous methylene blue by anatase TiO_2, optimization of the parameters increases the rate by nearly a factor of 3. The concept should extend to many photocatalytic materials and reactions.

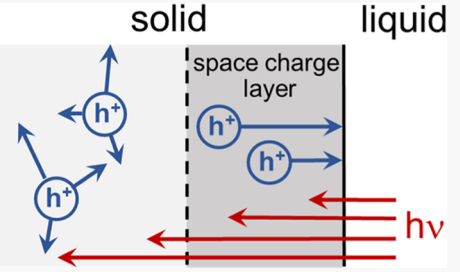

INTRODUCTION

Many material properties influence the photocatalytic efficacy of an oxide semiconductor, including the recombination time, absorptivity of light, and rate of carrier transport to the surface. Large bodies of published work describe approaches to improve the first two properties,[1,2] but less attention is focused upon carrier transport rates. In principle, transport driven by drift from electric fields can dwarf that from carrier diffusion. However, little attention has been paid to such effects because in devices such as fuel cells, supercapacitors, and photovoltaic devices that operate within liquid media of high ionic strength, drift-driven transport may be neglected.[3,4] The fluid medium homogenizes the electric potential throughout the solid network and eliminates internal electric fields.

However, such homogenization does not occur in certain important applications of photocatalysts. For example, non-porous polycrystalline films find use in self-cleaning windows and other weather-exposed surfaces[5,6] and in antimicrobial[7] and antifouling coatings.[8] In such films comprising anatase TiO_2,[9] the electric field generally $\mathcal{E}$ points outward from the solid, encompasses a space charge width w up to several hundred nanometers, and draws minority carriers toward the surface to increase the reaction rate. Figure S1 in the Supporting Information illustrates the relevant electronic band diagram.

Mesoporous sintered films operating in gases or liquids of low ionic strength should exhibit analogous behavior. Individual particles are too small to support noticeable electric fields across their diameters.[10] However, electrical connectivity within the network enables creation of a field extending over many particle diameters having its principal component directed perpendicular to the nominal film surface. For anatase TiO_2, this connectivity occurs under ultraviolet (UV) illumination even for loosely aggregated particulate films because of an autodoping effect.[11] A field of suitable sign and direction could pull photocarriers toward the nominal surface faster than the fluid reactant diffuses into the porous network. Higher reactant concentrations exist at the nominal surface than within the network, so the overall photoreaction rate should increase. This approach would mitigate some of the fluid diffusion limitations that limit reaction rates, especially in liquids, and also avoids the cost of filtering freely suspended particles[1,2,12−15] from the reactor effluent.

The present work demonstrates the workability of this concept for thin films of porous anatase TiO_2 that catalyze the photo-oxidation of aqueous methylene blue (MB). $\mathcal{E}$ is manipulated by methods for defect engineering that vary the donor concentration N_d and the built-in potential V_S at the nominal free surface. Indeed, the methods enable considerable decoupling between these two parameters, so their effects may be examined in isolation. The reaction rate varies with N_d and V_S in directions and with magnitudes consistent with the predictions of a straightforward photocurrent model. Physical, chemical, and electrical characterization reveals no discernible changes in catalyst properties other than N_d and V_S.

Conceptual Background. In a semiconductor without internal electric fields, only minority carriers generated within about one diffusion length L_p of a surface will reach it. However, in thin films, illumination creates photocarriers much deeper in the material, down to roughly the penetration depth

Received: October 16, 2021
Revised: December 28, 2021
Published: January 11, 2022

https://doi.org/10.1021/acs.jpcc.1c09020
J. Phys. Chem. C 2022, 126, 1376−1388

of light. In anatase, for example, L_p is about 10 nm,[9,16,17] but the penetration depth at a wavelength of 360 nm is in the order of 1000 nm. To use these minority carriers for reaction, a suitably directed electric field must exist internally to the semiconductor that reaches well beyond L_p.

Suspended particles are too small to support significant electric fields, but photoreaction still occurs readily because particle radii are in the order of L_p.[23−27] Such particles have a high specific surface area but require filtration from the reaction effluent. The nonporous polycrystalline material supports internal fields. The specific surface area is rather small, however, and films can be relatively expensive to fabricate. Mesoporous films represent an intermediate case in the continuum from suspended particles to the nonporous polycrystalline material. Figure 1 shows a schematic diagram

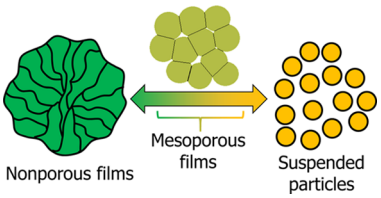

Figure 1. Conceptual continuum between uniform medium and suspended particles.

representing this idea. Sintered porous films eliminate the need for filtration and offers a high specific surface area and adequate electrical connectivity for electric fields to develop on length scales spanning many particle diameters.

The presence of such electric fields enables manipulation of photocarrier movement by use of layered structures (as in BiOX (X = Cl, Br, and I) nanomaterials[18,19]) and specific forms of defect engineering.[20] Substantial improvements in the photoreaction rate have been demonstrated in nonporous anatase[9,21] by defect engineering to control N_d and V_S. The grains within a nonporous polycrystalline semiconductor have a good electrical contact with each other and act as uniform medium to support a built-in space charge region encompassing many crystallites.[9] The width w of this region varies with N_d and V_S according to

$$w = \sqrt{\frac{2\varepsilon_s\varepsilon_0 V_s}{qN_d}} \quad (1)$$

where ε_0 is the vacuum permittivity; ε_s is the relative dielectric constant for the solid; and q is the charge on an electron. In anatase, typical carrier mobilities and lifetimes yield drift distances in the order of 1−10 μm,[9] far exceeding w. Thus, nearly all photocarriers generated within a depth w drift to the surface—a phenomenon that has been noted for various semiconductors including anatase.[9,21,22] A larger value of w yields an expanded volume from which generated photocarriers can reach the surface for reaction.

Equation 1 indicates that w increases with the square root of V_S and inversely with the square root of the donor concentration. N_d can be manipulated by engineering the concentration of electrically active native and extrinsic defects within the crystallites and at their boundaries.[9] V_S can be manipulated by defect engineering within the first few nanometers near the surface.[21] For anatase, the engineered values of V_S appeared to remain robust against shifts[23] resulting from effects such as light-induced band flattening and adsorption.

If the minority carrier lifetime is sufficiently large in a mesoporous film, a large value of w may yield benefits through adjustment of N_d and V_S akin to nonporous films. In anatase, wherein the minority carriers are typically holes, the lifetime varies widely depending upon the preparation procedure, interfacial charge transfer rates, use of geometries such as nanotubes that promote electron−hole separation,[17] and other factors.[23] However, as a working hypothesis, it is plausible to suppose that the carriers generated within depth w last long enough to drift to the nominal film surface. The reactant concentration is greater here than deep within the porous structure.

The approach discussed here focuses on minority carriers and therefore differs in important respects from the techniques employed in majority-carrier devices such as solar cells. In such devices, attempts to improve majority-carrier electron transport have focused on approaches such as using one-dimensional nanotubes, nanorods, or nanowires to limit random diffusion within a wide network and to suppress impeded transport at intercrystalline contacts.[28] Internal electric fields have played a smaller role.

METHODS

Material Synthesis. The synthesis method sought to create films of sintered anatase particles on flat substrates of electrically conductive fluorine-doped tin oxide (FTO). This configuration permits electrical characterization of the semiconductor's donor concentration. To this end, FTO-coated glass slides (Sigma-Aldrich, SnO_2/F, 7 Ω/sq surface resistivity, 80−82%transmittance) were coated with a slurry of anatase nanoparticles (Nanostructured & Amorphous Materials, Inc., 10 nm average diameter). The slurry preparation procedure was adapted from the published literature[29] and began with grinding 3 g of anatase in a porcelain mortar/pestle together with 1 mL of deionized water, 0.1 mL of acetylacetone (Sigma-Aldrich), 4 mL of deionized water, and 0.1 mL of Triton X-100 (Sigma-Aldrich) that were added sequentially. The slurry was then applied to the FTO by the doctor blade method, allowed to dry in air for 30 min, and sintered in air for 6 h in a furnace. The sintering temperature of 500 °C avoided the crystalline-phase transformation to rutile.[30,31] The unwanted material was then removed to obtain a coated area of 1 cm × 1 cm.

Manipulation of the Donor Concentration and Built-In Potential. Slight chemical reduction of anatase by annealing in H_2 enabled manipulation of the donor concentration N_d. Annealing was performed in a small (0.2 L) stainless-steel chamber that was evacuated using a mechanical pump. Specimens prepared as described above were heated by affixing them to an electrically conductive back plate cut from an n-type (Sb doped, 0.013 Ω cm) Si(100) wafer. Bonding was accomplished with a ceramic adhesive (Aremco ULTRA-TEMP 516). The ends of the Si back plate were wrapped with tantalum foil (Sigma-Aldrich, 0.25 mm thick) to improve the contact resistance between the plate and copper support rods that provided electrical current for resistive heating. Annealing was performed at 500 °C for 1 h in partial pressures of H_2 ranging from near zero to 20 mTorr. Temperature was monitored with a chromel−alumel (type K) thermocouple press-fitted to each specimen.

Exposure of the anatase film to a controlled flux of hydrogen ions enabled variation of the built-in potential V_S at the film's

https://doi.org/10.1021/acs.jpcc.1c09020
J. Phys. Chem. C 2022, 126, 1376−1388

nominal surface. This exposure was accomplished in an apparatus designed specifically for plasma treatment coupled with *in situ* surface analysis.[32] The main body of the chamber was constructed with stainless steel and was equipped with a load lock, specimen transfer arrangement, and hemispherical analyzer for X-ray photoelectron spectroscopy (XPS). Specimens were mounted at ground potential on a molybdenum holder using double-sided copper tape and a molybdenum clip.

The remote plasma discharge was energized using a 2.45 GHz electron cyclotron resonance source. The deuterium isotope of hydrogen was employed rather than H_2 because D_2 provided a more stable plasma at the operating pressure of 1.7×10^{-3} to 1.9×10^{-3} Torr. Molybdenum grids were placed between the plasma and the specimen. In some cases, voltages were applied to these grids such that ions (mainly D_2^+) were accelerated to 100 eV before striking the specimen surface. In other cases, the grids were grounded to avoid acceleration. Biased conditions enabled access to higher values of V_S than unbiased. In both cases, measurement of electrical current through the specimen yielded an incident ion flux of 1.6×10^{13} cm^{-2} s^{-1}. Simulations employing the TRIM package[33] indicated an ion penetration depth of 2.7 nm under biased grid conditions.

Material Characterization. X-ray diffraction patterns were measured using a PANalytical/Philips X'pert Materials Research diffractometer using a Cu Kα_1 source at 0.154056 nm. The surface area and pore size distribution were, respectively, measured by the Brunauer–Emmett–Teller and Barrett–Joyner–Halenda methods,[34,35] using N_2 as the adsorbing gas in a Quantachrome NOVA 2200e surface area analyzer. The film thickness was measured using a Sloan Dektak 3ST profilometer with 2.5 μm-radius conical-shape stylus (cone angle of 90°). The optical absorption in the UV–near-infrared range was measured with a Cary 5000 spectrophotometer. Absorption spectra were computed by difference between FTO substrates with and without the anatase films.

Electrochemical impedance spectroscopy (EIS) provided values for N_d. A three-electrode electrochemical cell employed the anatase film as the working electrode, Pt as the counter electrode, and Ag/AgCl as the reference electrode. The aqueous electrolyte was 0.1 M Na_2SO_4 saturated with Ar gas. A potentiostat (BioLogic Science Instruments model SP150) accomplished the measurement at a frequency of 1 kHz with a modulation amplitude of 10 mV. Calibration of the Ag/AgCl electrode and cleaning of the Pt electrode were performed before each measurement. The cell circuit model assumed Ohmic contacts and components everywhere except for a capacitive Schottky contact at the semiconductor–electrolyte interface. The measured capacitance includes contributions in series from a semiconductor space charge layer (SCL) and a Helmholtz liquid layer, although the semiconductor capacitance dominates at the frequency of measurement.[36] An assumed dielectric constant of 55[37] for anatase then yields N_d through the Mott–Schottky relation.

XPS measurements for precisely determining the valence band edge in an untreated material were performed using a Kratos Axis Ultra X-ray photoelectron spectrometer (Kratos Analytical, Inc., Manchester, UK) with monochromatic Al Kα radiation (1486.6 eV). High-resolution spectra were collected with a pass energy of 20 eV and an energy step of 0.1 eV using a hybrid (electrostatic and magnetic immersion) lens mode. The analyzer specific zero binding energy was set using the Fermi edge of a gold foil. Although the electron neutralizer was employed to compensate electron loss, specimens were loaded onto copper tape with the FTO surface secured using a copper clip to help reduce the charging effects.

In situ XPS measurements were used to gauge the valence band position and chemical composition before and after plasma treatment. A hemispherical analyzer (SPECS 150 EP) was operated with a SPECS XR50 X-ray source. Spectra were collected using Al Kα radiation (1486.6 eV) with a pass energy of 50 eV and an energy step of 0.1 eV. Every experiment included a survey encompassing the O 1s, Ti 2p, and C 1s transitions and the valence band edge. Specimen charging effects occurring before plasma treatment were calibrated using the adventitious C 1s peak at 284.8 eV. Plasma treatment distorted this peak, however, so post-treatment calibration employed the Ti $2p_{3/2}$ peak characteristic of anatase with a small shoulder from Ti_2O_3 added. The movement of the valence band edge was monitored using methods described elsewhere,[21] with details given in the Supporting Information.

Reaction Rate Measurement. The apparent first-order reaction rate constants k_{app} were measured using the test reaction of MB photo-oxidation, which exhibits well-known pseudo-first-order kinetics. Rates were measured in a small batch reactor, with the specimens illuminated through a quartz window using a solar-simulating light source providing a total broadband intensity of 370 mW/cm^2. In each experiment, the concentration of MB was monitored as a function of time by continuous UV–visible absorption external to the reactor at 356 nm, with flow through the external tubing driven using a peristaltic pump. Various calibration measurements corrected for the homogeneous reaction of MB, long-term drifts in illumination intensity, and related effects.

Flow within the reactor arising from the external sampling apparatus provided considerable convective mixing to homogenize the reactant concentration. Molecular diffusion also promoted good reactant mixing, as shown by the following estimate. The reaction typically ran for a time t near 6 h, and the diffusivity of MB in water is $D = 4 \times 10^{-6}$ cm^2/s.[38] The corresponding diffusion length l during the experiment is $l^2 = 6Dt$, yielding $l = 0.58$ cm. This length roughly equaled the internal width of the reactor.

Since adsorption of MB on anatase occurs slowly, 1 h of adsorption equilibration between the MB solution and the TiO_2 was allowed before photocatalytic measurements. The MB absorbance of 665 nm indicated successful establishment of equilibrium within this period, consistent with the published literature for MB and anatase.[39] As discussed in the Supporting Information and observed elsewhere in the literature,[40−43] MB decomposition proceeded according to pseudo-first-order kinetics under the conditions of the experiment. Initial preparation of the reaction mixture provided ample opportunity for equilibration between dissolved O_2 and ambient air, and the reaction apparatus allowed for entry of O_2 during light exposure. Thus, the photobleaching mechanism should be oxidative rather than reductive.[44]

Liquid-phase diffusivities vary inversely with the fluid viscosity according to the Stokes–Einstein relationship. To investigate the effects of such diffusivity variation, experiments were done with a film untreated with hydrogen annealing or plasma, in which polyethylene glycol 2000 (Sigma-Aldrich, molecular weight = 1800 g/mole) was added to the reaction mixture. Varying amounts of thickener were added that sufficed to yield polymer mass fractions up to 0.2, which

https://doi.org/10.1021/acs.jpcc.1c09020
J. Phys. Chem. C 2022, 126, 1376−1388

decreases the diffusivity by a factor of up to 5. Control experiments indicated that the solution viscosity did not change during photoreaction.

RESULTS

Physical and Chemical Characterization. Figure 2 shows example TEM micrographs of anatase nanoparticles

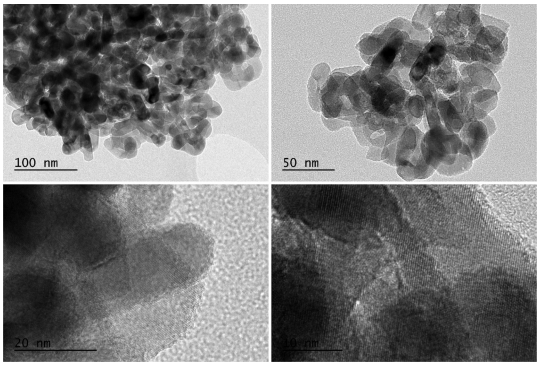

Figure 2. Transmission electron micrograph of suspended TiO_2 anatase particles at length scales ranging from 100 to 10 nm.

before sintering and confirms an average particle diameter of about 10 μm. Profilometry measurements after film synthesis and sintering reveal a thickness of 13−17 μm as shown in Figure 3. The roughness of 3.1 μm is sizable and accords with plan-view SEM (Figure 4), showing an average grain size near 0.5 μm. A sizable number of grains exhibit diameters above 1 μm.

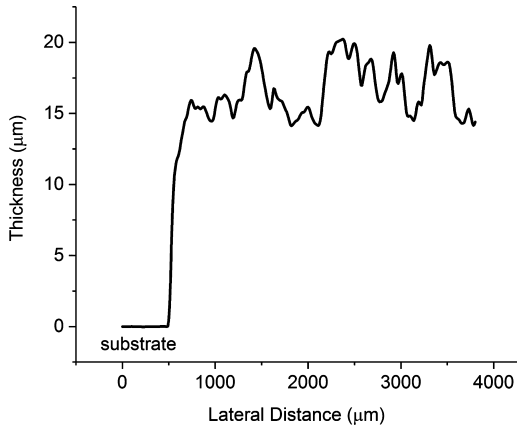

Figure 3. Profile measurement of a typical sintered anatase film.

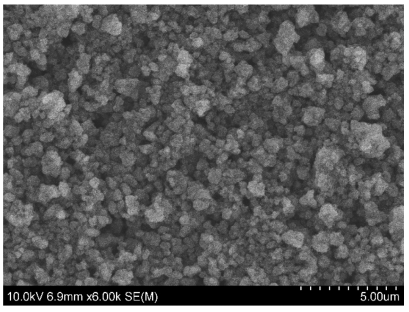

Figure 4. Scanning electron micrograph of a typical sintered anatase film.

Figure 5 shows an example X-ray diffraction pattern for a sintered film. The pattern includes contributions from TiO_2

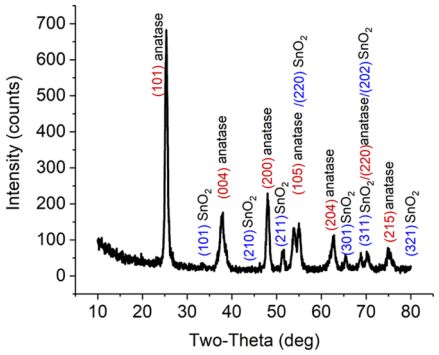

Figure 5. Example X-ray diffraction pattern of a typical sintered anatase film on FTO.

and SnO_2 in the underlying FTO. No TiO_2 phases were observed other than anatase, either before or after annealing in H_2. TiO_2 peaks were identified with JCPDS card number 00-021-1272 (tetragonal, a = 3.7852, c = 9.5139), and SnO_2 peaks were identified with JCPDS card number 04-003-0649 (tetragonal, a = 4.7371, c = 3.1851).

Table 1 shows the surface area and pore characteristics from N_2 adsorption measurements before and after sintering the

Table 1. Area and Pore Characteristics of Anatase Films

	unsintered	sintered
surface area (m^2/g)	91.1	78.9
pore volume (cc/g)	0.36	0.31
porosity (%)	33.8	23.0
pore radius (nm)	4.87	4.88

films. Sintering reduces the surface area by 13%, the pore volume by 14%, and the porosity by nearly one-third. However, the average pore radius remains about constant.

Chemical reduction by hydrogen annealing sought to affect N_d but not the fundamental atomic structure of the anatase. The procedure increases N_d because the anatase loses oxygen, which forms native point defects such as Ti interstitials and/or O vacancies that act as donors. However, extensive reduction of anatase leads to additional peaks, its X-ray patterns corresponding to new phases.[45,46] Such new phases were not desired here, and no peaks other than those of anatase were observed in response to the mild hydrogen reduction. Moreover, UV−visible absorption spectra (Figure 6) showed much less perturbation after mild hydrogen reduction than in the literature employing extensive reduction that leads to new phases.

Figure 7a shows the XPS survey scans of the sintered film before and after 0.5 h of plasma treatment. Binding energies were aligned using the C 1s graphitic carbon peak at 284.6 eV. The Ti 2p and O 1s peaks are clearly visible. Figure 7b−d shows the C 1s, O 1s, and Ti 2p peaks in more detail. The C 1s peaks decrease in size upon treatment, presumably due to some volatilization of the C. In addition to the large graphitic peak, there may be two smaller unresolved peaks associated with C−O (286.2 eV) and carbonyl (288.1 eV).[47−50] Treatment induces no new shoulders or other chemical shifts. The O 1s peak has a poorly resolved shoulder above the main peak at 529.7 eV. The shoulder may include contributions

https://doi.org/10.1021/acs.jpcc.1c09020
J. Phys. Chem. C 2022, 126, 1376−1388

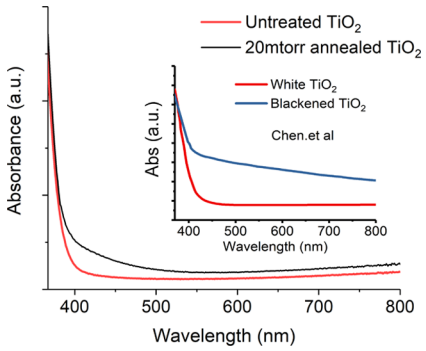

Figure 6. UV−visible absorption spectroscopy of a typical sintered anatase film, compared with literature data for strongly reduced anatase shown in the inset (data taken and adapted from ref 46).

from OH groups existing as Ti−OH (533.5 eV) or OH at bridging sites (531.5 eV).[51−54] The O 1s peaks grow slightly in size after treatment, presumably due to loss of partially obscuring carbon, but there is no obvious change in the peak shape. The Ti 2p peaks comprising Ti $2p_{3/2}$ and Ti $2p_{1/2}$ are located at 458.6 and 464.4 eV, respectively, with the peak areas in the expected 2:1 ratio. The Ti peak positions indicate an oxidation state of Ti^{4+}.[55] The lack of shoulders or asymmetry in the peaks suggests that little or no Ti^{3+} is present either before or after treatment. Akin to the behavior of the O 1s peaks, the Ti peaks grow in size after treatment but remain largely unchanged in shape.

In contrast, biased plasma treatment induces extensive chemical changes as shown in Figure 8 for Ti 2p. Two shoulders appear at lower binding energies alongside the two main peaks at 456.5 and 462.2 eV signifying the presence of Ti^{3+},[56,57] indicating that chemical reduction has taken place.

Electrical Characterization. Figure 9 shows an example Mott−Schottky plot employed for the determination of N_d. The curve shape behaves as expected for a depletion layer. Depletion layers are considered as the norm for anatase surfaces,[58] although accumulation layers have been observed

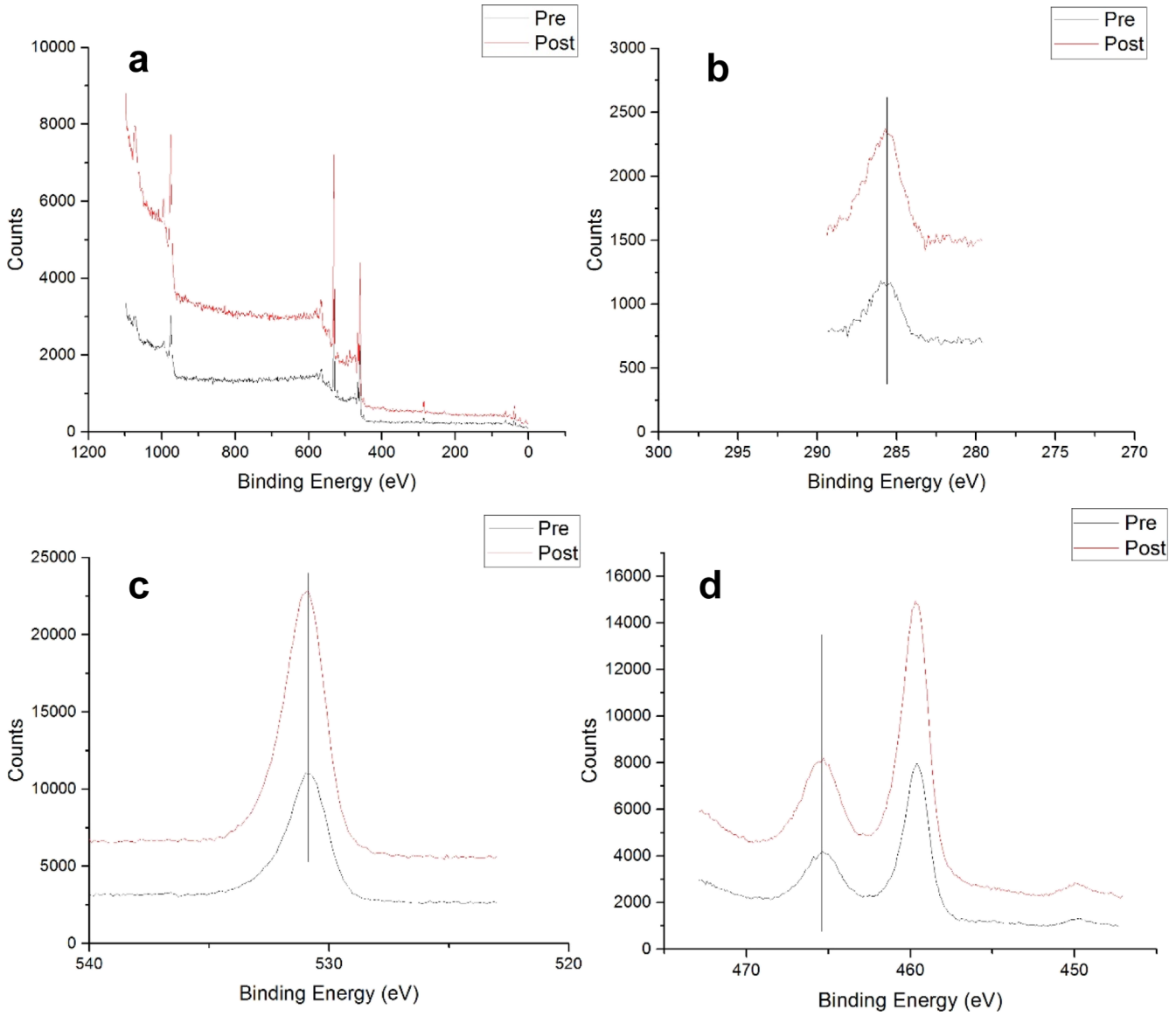

Figure 7. XPS shown before and after 0.5 h plasma treatment with no bias, including (a) survey spectra and close-ups of peaks for (b) C 1s, (c) O 1s, and (d) Ti 2p.

https://doi.org/10.1021/acs.jpcc.1c09020
J. Phys. Chem. C 2022, 126, 1376−1388

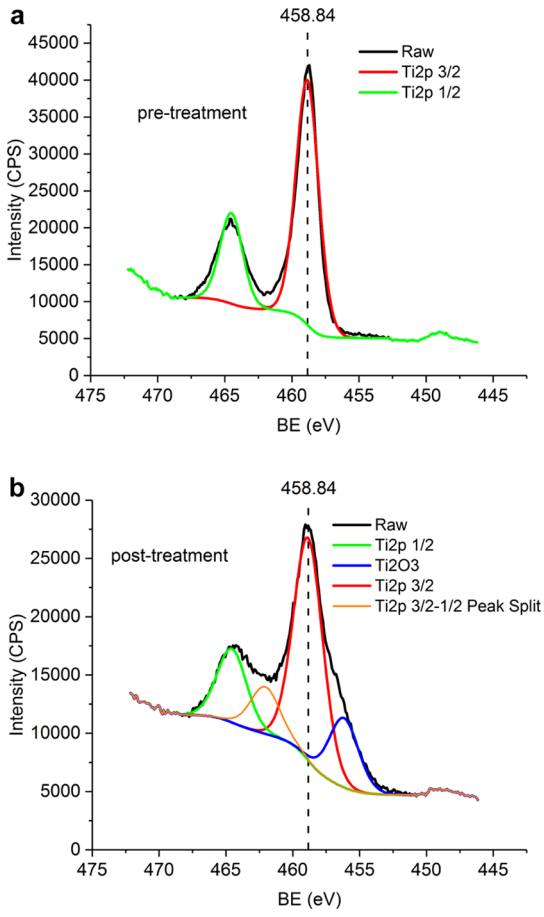

Figure 8. XPS Ti 2p peaks shown (a) before and (b) after 1 h of plasma treatment with 100 V bias.

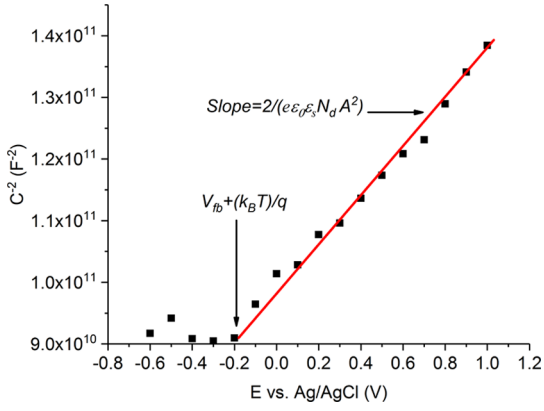

Figure 9. Example Mott–Schottky plot for the measurement of N_d of a sintered anatase film. In this case, $N_d = 5.3 \times 10^{19}$ cm^{-3}.

for anatase single crystals bombarded with 2 keV Ar ions and subsequently annealed in low-pressure O_2.[59]

The donor concentration computed from such plots for untreated films is 1.3×10^{17} cm^{-3}. Annealing in varying pressures of H_2 leads to progressively higher values of N_d up to 5.3×10^{19} cm^{-3}. Although this value exceeds that of the untreated material by 2 orders of magnitude, N_d remains much lower than the reported value for strongly reduced anatase (2.1×10^{22} cm^{-3}).[45,46] Mild reduction conditions also lead to a decrease in V_S from 0.31 to 0.18 eV (Figure 10). This decrease results from the increase in N_d, which induces the Fermi

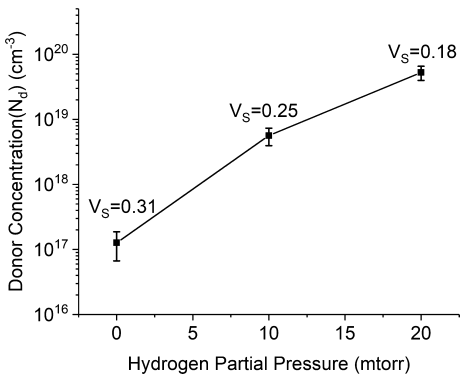

Figure 10. Dependence of N_d on hydrogen annealing pressure. V_S changes with N_d because the Fermi level moves within the bulk but remains pinned at the surface.

energy in the bulk to rise by about 0.15 eV assuming that the surface Fermi energy remains constant. In other words, varying N_d unavoidably leads to modest changes in V_S as well.

Plasma exposure sought to induce the formation of electrically active point defects within 2–3 nm of the surface in order to move the Fermi energy at the surface without changing N_d deeper in the bulk. Only the nominal free surface was exposed to H radicals or ions; internal pore surfaces remained unaffected. For the specific surface area reported in Table 1 for sintered films, the internal reactive area in a layer of about 100 nm thickness (typical of the depletion widths used in this work) is larger than the nominal free surface area by roughly a factor of 30. Figure 11 shows that V_S increases by up

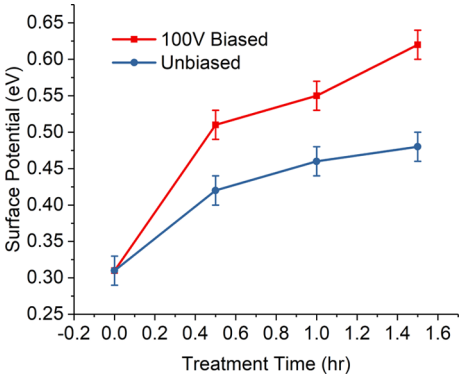

Figure 11. V_S vs plasma treatment time under biased and unbiased conditions. Biasing broadened the range over which V_S could be varied.

to a factor of about 2 depending upon the treatment time and biasing conditions, from 0.31 to 0.62 eV. The largest change takes place under biased conditions, although the unbiased plasma still induces significant increases.

Hydrogen exists in several forms in anatase.[60,61] Hydrogen atoms present as interstitials or bonded to O vacancies act as shallow donors, while interstitial H_2 is electrically inactive. Hydrogen donors do not appear to dominate the behavior of V_S here, as the increasing values signify movement of the surface Fermi energy toward the mid-gap instead of toward the conduction band. However, complexation of hydrogen with oxygen vacancies and extrinsic defects may change their donor properties and give rise to the observed changes.

https://doi.org/10.1021/acs.jpcc.1c09020
J. Phys. Chem. C 2022, 126, 1376–1388

Reaction Rate Measurements. The value of k_{app} for MB photo-oxidation decreased in response to increases in N_d by a factor of 2.3, from 0.093 to 0.040 h^{-1}(Figure 12a). Increasing V_S caused k_{app} to rise by about 25% (Figure 12b). It is evident that an increase in V_S caused k_{app} to move in the opposite direction from an increase in N_d.

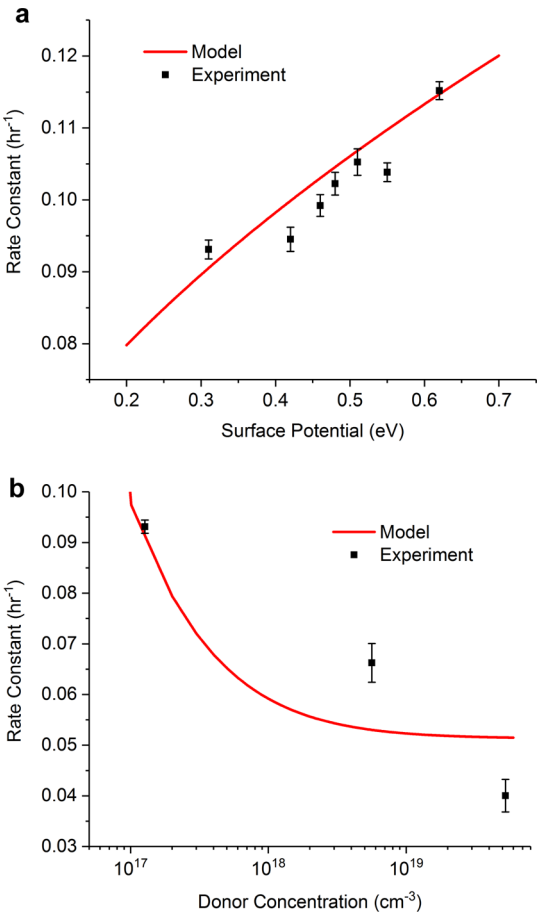

Figure 12. Apparent rate constant k_{app} vs (a) V_S and (b) N_d. Data points corresponding to the untreated catalyst are at V_S = 0.3 V in (a) and N_d = 1.3 × 10^{17} cm^{-3} in (b).

Polyethylene glycol was added to the liquid phase in order to decrease the diffusivity of MB by a factor of up to 5,[62] from 1.3 × 10^5 to 0.27 × 10^5 nm^2/s. Measurements with a mass fraction of 0.2 showed a decrease in k_{app} by about 20%, from 0.093 to 0.074 h^{-1} (Figure 13) A mass fraction of 0.1 decreased k_{app} by most of this amount to 0.077 h^{-1}.

DISCUSSION

The utility of TiO_2 as a photocatalyst is hampered by limited absorption of the solar spectrum[46,63−66] and fast recombination of charge carriers.[65,67−72] Common methods to improve optical absorption include blackening through hydrogenation[46,73−75] and by doping with foreign elements to shrink the band gap. Methods to lessen recombination include co-doping and placement of metal nanoparticles on the surface.[76,77] The present work uses a different approach that seeks to use photocarriers more efficiently by actively sweeping them toward the surface by building in an electric field.

Model for Combined Carrier−Reactant Diffusion and Reaction. The one-dimensional, steady-state treatment

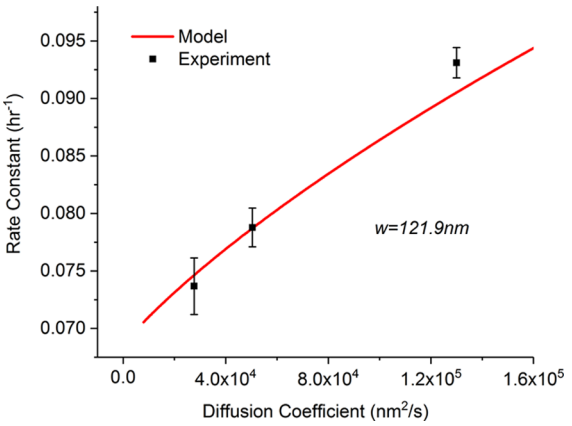

Figure 13. Apparent rate constant k_{app} vs D_{pore} for the untreated film.

integrates an analytical description of diffusion and reaction in porous catalysts with a photocurrent model for photocatalysis by nonporous films. The following paragraphs describe the model's most important features, with additional details appearing in the Supporting Information. We consider steady-state photocatalysis by a porous rectangular slab of thickness 2L with the center line at x = 0, specific area per unit volume A (m^2/m^3), and nominal film area A_{nom} on each side of the slab. Figure 14 sketches the reactant concentration versus depth, with the reaction taking place at the film's surface at L and also within the field-free pores between x = 0 and $x = L - w$.

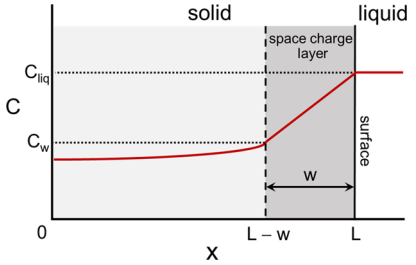

Figure 14. Schematic of MB concentration vs depth within the film. The zero is set at the interface between the film and its mechanical support, so that the surface resides at $x = L$. The SCL of width w therefore stretches between the surface at L and $L - w$.

The total reaction rate R_{total} (moles/s) in the film comprises a drift component R_{drift} from photocarriers that react at the film surface and a pore component R_{pore} from photocarriers generated beyond the SCL that diffuse to nearby pore walls. As the Supporting Information shows in more detail, the drift contribution to the total rate obeys

$$R_{drift} = kAC_{liq}A_{nom}w \tag{2}$$

where k denotes the rate constant per unit internal area of pores (s^{-1} m^{-2}). For the pore component, analytical expressions for the effectiveness factor of heterogeneously catalyzed reactions simplify the computation as shown in the Supporting Information. The reactant concentration C_w at the edge of the SCL becomes

$$C_w = \frac{C_{liq}}{1 + w\sqrt{\frac{kA}{D_{pore}}}\tanh\left[(L - w)\sqrt{\frac{kA}{D_{pore}}}\right]} \tag{3}$$

https://doi.org/10.1021/acs.jpcc.1c09020
J. Phys. Chem. C 2022, 126, 1376−1388

A Thiele modulus Φ may be defined for the field-free region as

$$\Phi = (L - w)\sqrt{kA/D_{pore}} \quad (4)$$

with the corresponding effectiveness factor η given by

$$\eta = \frac{\frac{1}{L-w}\int_w^L r(x)\mathrm{d}x}{r(C_w)} = \frac{\tanh(\Phi)}{\Phi} \quad (5)$$

In a reactive volume that equals $A_{nom}(L - w)$, R_{pore} becomes

$$R_{pore} = \eta k A A_{nom}(L - w)C_w \quad (6)$$

The total reaction rate for comparison with experiment combines the expressions for R_{drift} and R_{pore}

$$R_{total} = R_{drift} + R_{pore} = kAA_{nom}[C_{liq}w + \eta C_w(L - w)] \quad (7)$$

The diffusivity D_{pore} invariably enters into the overall rate through the combined parameter k/D_{pore}. However, k appears by itself as the leading term in eq 7, enabling D_{pore} to be disaggregated from k. In the asymptotic limit of large w, R_{drift} dominates R_{total} and varies linearly with w. The effects of D_{pore} become negligible. This regime determines a unique value of k, which permits the determination of D_{pore} from k/D_{pore} in the asymptotic limit $w \to 0$ where pore diffusion dominates.

Fitting of the rate data to obtain D_{pore} and k was performed by minimizing an objective function S composed of equally weighted squared residuals

$$S = \sum (k_{app}^{exp} - k_{app}^{model})^2 \quad (8)$$

where k_{app}^{model} denotes the apparent rate constant computed from the model and k_{app}^{exp} denotes the corresponding quantity from experimental rates. The Supporting Information describes the procedures employed to determine confidence intervals for the fitted and derived parameters.

Comparison of the Model with Rate Data. The parameters detailed above fall into three categories: known from experimental conditions, fitted from rate data, and derived from the fitted parameters. Known parameters include not only N_d and V_S but also others shown in Table 2, such as L from profilometry, C_{liq} from the MB solution formulation, A from BET measurements, and A_{nom} from the choice of convenience. The model contains only two adjustable parameters to fit from rate data: D_{pore} and k. These two parameters work in concert with the known parameters to control k_{app} through the functional forms embodied in eqs 1−7. Since these function forms are rather complicated, the ability of the model to fit variations in k_{app} with N_d, V_S, and D_{pore} represents a significant test of the underlying physical picture. Parameters derived from k and D_{pore} include Φ and η.

Table 2. Known Parameters

parameter	value
L	13−17 μm
C_{liq}	1×10^{-5} mol/L
A	0.146 nm^2/nm^3
A_{nom}	1 cm^2 = 1×10^{14} nm^2

Table 3 shows the fitted and derived parameters. The best fit value of D_{pore} in water is $1.3 \times 10^{5 \pm 0.3}$ nm^2/s. A similar value of 4×10^5 nm^2/s was obtained for a related type of dye in an electrode incorporating TiO_2 particulates.[64] This correspondence provides evidence that the model captures the key physics and chemistry reasonably accurately. As expected for diffusion in confined spaces, both values lie considerably below the normal liquid phase value of $D = 4 \times 10^{-6}$ cm^2/s = 4×10^8 nm^2/s.[64]

Table 3. Fitted and Derived Parameters

parameter	value
D_{pore}	$1.3 \times 10^{5 \pm 0.3}$ nm^2/s
k	107 ± 2 nm/s
Φ	141
η	0.0071

The best-fit value of k is 107 nm/s under the illumination conditions employed. Variations in synthesis protocols and illumination intensity complicate direct comparison of this number to the literature. Comparison of the measured and modeled magnitude and direction of k_{app} with N_d and V_S is more instructive. Figure 12a,b shows these comparisons. For V_S, the model predicts a nearly linear increase in k_{app} by about 25% in a range over which V_S increases by a factor of about 2. The prediction captures both the magnitude and slope of the variation. Confidence intervals on the experimental points are too large to detect the slight curvature in k_{app} versus V_S predicted by the model. For N_d, the prediction captures the rough magnitude and general direction of the variation—a decrease in k_{app} by about a factor of 2 as N_d increases by a factor of 500. However, the data do not match the significant curvature predicted by the model.

For D_{pore} (Figure 13), the model predicts a nearly linear increase in k_{app} by about 25% in a range over which D_{pore} increases by a factor of about 3. As with V_S, the prediction for D_{pore} captures both the magnitude and slope of the variation, with confidence intervals for the data being too large to assess the slight curvature.

Polymers based on ethylene glycol are known to undergo photocatalytic degradation in the presence of TiO_2, yielding shorter glycol chains and a variety of esters and aldehydes.[78,79] Those studies were done at much lower polymer concentrations than employed here, with rates too low to change the solution viscosity in the present work. However, such reactions could conceivably compete with MB decomposition for photogenerated holes and thereby depress the rate constant k. As mentioned above, D_{pore} enters into k_{app} through the combined parameter k/D_{pore}. Increasing the polymer mass fraction from 0.1 to 0.2 decreases D_{pore} by a factor of about 2. Any simultaneous depression of k would compensate some of this decrease in D_{pore} and attenuate the change in k_{app} predicted by eqs 1−7. Indeed, if k decreases in direct proportion to the polymer concentration, the compensation would be complete and k_{app} would remain constant. However, Figure 13 shows that k_{app} decreases as predicted by eqs 1−7 with constant k. This result suggests that the polymer photoreaction does not influence the MB rate under the conditions of the experiment.

A fundamental premise of the model is that electric fields within the solid sweep most holes generated to a depth w toward the nominal free surface. In other words, w is a physical quantity more fundamental to photocarrier behavior than either N_d or V_S. It is therefore instructive to combine the data in Figure 12a,b into a single dataset plotted as a function of w according to eq 1. Figure 15 shows the experimental and

https://doi.org/10.1021/acs.jpcc.1c09020
J. Phys. Chem. C 2022, 126, 1376−1388

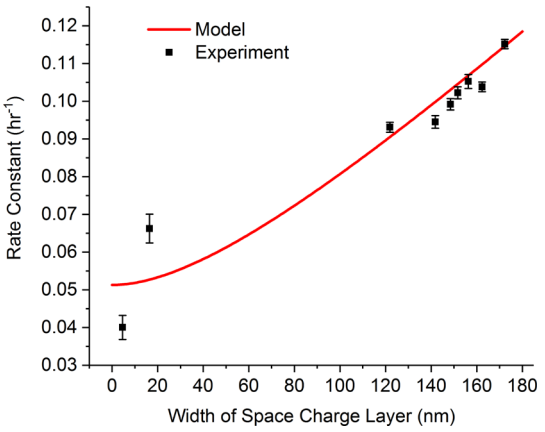

Figure 15. Apparent rate constant k_{app} vs width w of SCL. The untreated film corresponds to the data point at 122 nm.

model predictions in this way. As w increases from 5 to 180 nm, k_{app} increases by slightly over a factor of 2 for both the experimental data and predictions. Correspondence is best at large values of w and declines noticeably for small w. The data points at small w correspond to the largest values of N_d in Figure 12b, where deviations are also most pronounced.

Assessment of Model Assumptions. The physical picture underlying the model presupposes that the photoreaction by the diffusive motion of holes to particle sidewalls happens only deep within the film beyond the SCL width w. Holes generated within the SCL react not at the sidewalls but at the nominal surface under the influence of the electric field. A simple computation shows that this picture presupposes that the rate of hole loss by recombination or reaction at the sidewalls must be low enough to enable drift to dominate. The diffusion length x_{diff} can be estimated from

$$x_{diff} = \sqrt{\mu \frac{k_B T}{q} \tau} \tag{9}$$

where k_B represents the Boltzmann constant, T is the temperature, μ is the hole mobility, and τ is the time of diffusion. The drift length x_{drift} in an electric field $\mathcal{E}$ obeys

$$x_{drift} = \mu \mathcal{E} \tau \tag{10}$$

To compare x_{diff} and x_{drift} at a single value of τ, we can rearrange eqs 9 and 10 to yield

$$x_{drift} = \frac{q \mathcal{E} x_{diff}^2}{k_B T} \tag{11}$$

If we assume a particle radius of 5 nm for x_{diff} and a typical field strength in the order of 1 V/100 nm = 10^7 V/m at room temperature, eq 11 yields x_{drift} = 9 nm. This value is much smaller than the SCL width, so clearly drift cannot sweep holes far enough to reach the nominal surface if the efficiency of hole loss at the sidewall is high.

The efficiency of this loss for anatase particles is a complicated matter that has been reviewed extensively[23,80] and varies over orders of magnitude in colloidal and particulate systems. Loss rates depend upon surface preparation, the presence of electron scavengers, various trapping mechanisms, optical absorptivity, light intensity, and other factors. It is therefore plausible in the present system that surface loss may occur slowly enough for drift to dominate. Furthermore, it is difficult to rationalize the variation in k_{app} with V_S without invoking drift. Plasma treatment affects only the exposed free surface of the film, which as mentioned above comprises only a small percentage of the total reactive surface area. The XPS measurements show changes in the surface chemical composition with plasma treatment under bias with ions accelerated into the surface but not in the absence of bias. However, the data from biased and unbiased treatment all follow an unbroken pattern in Figure 12b—a pattern that furthermore aligns well with the picture embodied in eq 1.

The inability of the model to capture the behavior of k_{app} in some respects at high values of N_d deserves discussion. The mild hydrogen reduction employed to reach this regime could have changed some aspects of surface reactivity. Interstitial hydrogen atoms are unstable during long-term storage at room temperature[60] because a low diffusion barrier[81] enables disappearance to form interstitial H_2 or to bond with other intrinsic or extrinsic traps. However, the treatment does affect light absorption as shown in Figure 6, which may propagate into the efficiency of hole loss at the sidewalls. An equally likely explanation relates to the exceptionally small value of w in this range: only 5−20 nm. Grain sizes are much larger, averaging about 500 nm, with the roughness of the nominal surface near 3 μm. Given the mismatch in length scales and the complicated geometry of the nominal surface, it is perhaps notable that the model works modestly well.

Prospects for Generalizing the Concept. The concept for influencing the photoreaction rate via w through defect engineering to control N_d and V_S (i.e., via eq 1) has been demonstrated previously for nonporous anatase.[9,21] The present work suggests that these concepts extend to porous anatase and likely to photo-oxidations other than MB, although according to a different quantitative description that includes liquid-phase transport. Defect engineering of nonporous anatase relied upon specialized synthesis methods using amorphous TiO_2 (for N_d) and treatment with O_2 plasma (for V_S). The effects of synthesis from amorphous TiO_2 are complicated to implement and depend upon film thickness, while O_2 plasma treatment induces a decrease in V_S rather than an increase. The present work therefore employs different approaches involving hydrogen: thermal annealing (for N_d) and treatment with D_2 plasma (for V_S). However, thermal annealing in H_2 decreases the rate unhelpfully. Moreover, hydrogen-based methods entail complications that arise from competition between incorporation of hydrogen and formation of interface or bulk defects.[82−84] Under some circumstances, anatase photocatalysts treated with hydrogen exhibit deactivation over time.[84,85] The effects are complex and require further study before practical implementation.[86,87]

In short, for both nonporous and porous anatase, improvements are required in defect engineering methods to stably and simultaneously decrease N_d and increase V_S. The plasma method employed here was able to raise V_S by a few tenths of a volt. Whether other methods could generate larger changes remains a matter of speculation. However, band bending larger than a semiconductor's band gap is very unlikely. Surface Fermi level pinning near the mid-gap is more common, which would limit V_S for anatase to about 1.6 V. This is a factor of only ~2.5 greater than obtained here, leading from eq 1 to a possible rate enhancement of about 1.6. Much larger enhancements would become possible if N_d could be decreased by 1 or more orders of magnitude. This would require methods for defect engineering capable of neutralizing or compensating the many kinds of donor species in anatase, including native Ti

https://doi.org/10.1021/acs.jpcc.1c09020
J. Phys. Chem. C 2022, 126, 1376−1388

interstitials, O vacancies, adventitious H, and other foreign impurities. Such attempts have been made,[88,89] although the methods remain far from mainstream.

The model developed here indicates that lower diffusion coefficients inhibit R_{pore}, while R_{drift} remains unaffected. Thus, tailored electric fields provide the greatest benefit when used for fluid reactions involving small diffusion coefficients. Figure 16 shows predictions for k_{app} over a wide range of pore

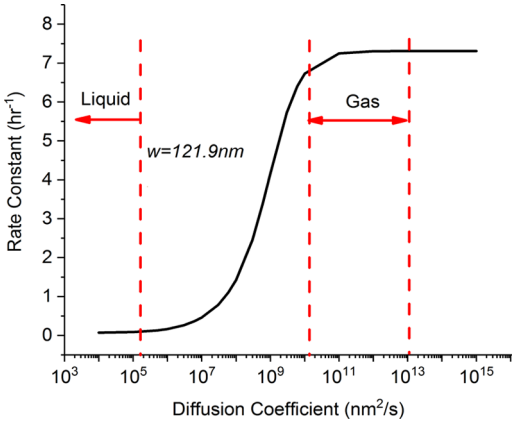

Figure 16. Model prediction for the apparent rate constant vs D_{pore}.

diffusivities encompassing both liquids and gases. Gases have much higher diffusivities; in porous media, Knudsen diffusion coefficients typically lie in the range from 10^{10} to 10^{13} nm^2/s[74,75,90,91] This range is several orders of magnitude higher than for water.[38,62] Maximal reactant concentrations therefore exist throughout the porous network, so the beneficial effects of electric field manipulation largely disappear because they become superfluous. Accordingly, defect engineering to increase w is likely to be helpful for liquids but not for gases.

Much attention in photocatalysis focuses on separating electrons and holes to preserve the minority holes for useful photoreaction. The field within the SCL does serve in this role; photogenerated holes deep within the semiconductor separate from the majority electrons residing there by sweeping the holes to the surface. However, the approach described here does not address the lateral separation on the nanometer length scale that is crucial for efficient photocatalysis, wherein oxidation and reduction reactions occur in close atomic-scale proximity to each other. Crystal facets, cocatalysts, and localized doping are the most common means to accomplish such separation,[92] although nanotubes are also attracting increasing attention.[17] The present approach implemented in a three-dimensional network sweeps holes in a direction normal to the surface. Upon arrival, they may be separated laterally by other means. This conceptualization in terms of a sequence of discrete transport steps is not precisely accurate in regions very close to the surface, but in three-dimensional networks, it may be useful to view the SCL-mediated transport as lying largely upstream of the lateral separation. In one- or two-dimensional geometries involving nanotubes or two-dimensional BiOX structures, the lateral separation begins much deeper within the solid. However, it is still helpful to view as conceptually distinct the separation that sweeps holes in the normal direction toward the surface.

CONCLUSIONS

This work provides substantial evidence that photoreaction rates in mesoporous films of semiconducting oxides can be increased through defect engineering that creates combinations of donor concentration and surface potential that yield wider space charge widths. Increased widths sweep more photocarriers to the nominal free surface where the reactant concentration is highest. Although this work has demonstrated the plausibility of the concept, the defect engineering techniques employed here acted only to increase N_d, which decreases the space charge width. Given the limited range of values available for varying V_S, full exploitation of this concept requires defect engineering methods capable of substantially decreasing N_d.

ASSOCIATED CONTENT

Supporting Information

The Supporting Information is available free of charge at https://pubs.acs.org/doi/10.1021/acs.jpcc.1c09020.

Method details for determining V_S; method details for measuring reaction rates; derivation of the model for combined carrier−reactant diffusion and reaction; and procedure for parameter fitting (PDF)

AUTHOR INFORMATION

Corresponding Author

Edmund G. Seebauer − *Department of Chemical and Biomolecular Engineering, University of Illinois, Urbana, Illinois 61801, United States;* orcid.org/0000-0002-4722-3901; Email: eseebaue@illinois.edu

Author

Qilong Huang − *Department of Chemical and Biomolecular Engineering, University of Illinois, Urbana, Illinois 61801, United States*

Complete contact information is available at: https://pubs.acs.org/10.1021/acs.jpcc.1c09020

Notes

The authors declare no competing financial interest.

ACKNOWLEDGMENTS

This work was partially supported by the National Science Foundation (DMR 13-06822 and 17-09327). The authors gratefully acknowledge Prof. J. P. Allain at the University of Illinois at Urbana-Champaign (UIUC) for use of the IGNIS (Ion-Gas-Neutral Interactions with Surfaces) system for plasma treatment and surface analysis. The authors also express special gratitude to Prof. A. A. Gewirth at the UIUC for use of his EIS apparatus.

REFERENCES

(1) Gaya, U. I.; Abdullah, A. H. Heterogeneous Photocatalytic Degradation of Organic Contaminants over Titanium Dioxide: A Review of Fundamentals, Progress and Problems. *J. Photochem. Photobiol., C* **2008**, *9*, 1−12.

(2) Nakata, K.; Fujishima, A. TiO_2 Photocatalysis: Design and Applications. *J. Photochem. Photobiol., C* **2012**, *13*, 169−189.

(3) Nelson, J. Continuous-Time Random-Walk Model of Electron Transport in Nanocrystalline TiO_2 Electrodes. *Phys. Rev. B: Condens. Matter Mater. Phys.* **1999**, *59*, 15374−15380.

(4) Schwarzburg, K.; Willig, F. Origin of Photovoltage and Photocurrent in the Nanoporous Dye-Sensitized Electrochemical Solar Cell. *J. Phys. Chem. B* **1999**, *103*, 5743−5746.
(5) Fujishima, A.; Hashimoto, K.; Watanabe, T. *TiO_2 Photocatalysis: Fundamentals and Applications*, 1st ed.; Bkc: Tokyo, 1999.
(6) Paz, Y.; Luo, Z.; Rabenberg, L.; Heller, A. Photooxidative Self-Cleaning Transparent Titanium Dioxide Films on Glass. *J. Mater. Res.* **1995**, *10*, 2842−2848.
(7) Chung, C.-J.; Lin, H.-I.; Tsou, H.-K.; Shi, Z.-Y.; He, J.-L. An Antimicrobial TiO_2 Coating for Reducing Hospital-Acquired Infection. *J. Biomed. Mater. Res., Part B* **2008**, *85*, 220−224.
(8) Yan, W.; Lin-lin, W.; Ming-yan, L. Antifouling and Enhancing Pool Boiling by TiO_2 Coating Surface in Nanometer Scale Thickness. *AIChE J.* **2007**, *53*, 3062−3076.
(9) Ong, S. W. D.; Lin, J.; Seebauer, E. G. Control of Methylene Blue Photo-Oxidation Rate over Polycrystalline Anatase TiO_2 Thin Films via Carrier Concentration. *J. Phys. Chem. C* **2015**, *119*, 11662−11671.
(10) Sodergren, S.; Hagfeldt, A.; Olsson, J.; Lindquist, S.-E. Theoretical Models for the Action Spectrum and the Current-Voltage Characteristics of Microporous Semiconductor Films in Photoelectrochemical Cells. *J. Phys. Chem.* **1994**, *98*, 5552.
(11) Wahl, A.; Augustynski, J. Charge Carrier Transport in Nanostructured Anatase TiO_2 Films Assisted by the Self-Doping of Nanoparticles. *J. Phys. Chem. B* **1998**, *102*, 7820−7828.
(12) Nosaka, Y.; Daimon, T.; Nosaka, A. Y.; Murakami, Y. Singlet Oxygen Formation in Photocatalytic TiO_2 Aqueous Suspension. *Phys. Chem. Chem. Phys.* **2004**, *6*, 2917−2918.
(13) Nosaka, Y.; Komori, S.; Yawata, K.; Hirakawa, T.; Nosaka, A. Y. Photocatalytic •OH Radical Formation in TiO_2 Aqueous Suspension Studied by Several Detection Methods. *Phys. Chem. Chem. Phys.* **2003**, *5*, 4731−4735.
(14) Linsebigler, A. L.; Lu, G.; Yates, J. T. Photocatalysis on TiO_2 Surfaces: Principles, Mechanisms, and Selected Results. *Chem. Rev.* **1995**, *95*, 735−758.
(15) Singh, A.; Kumari, S.; Shrivastav, R.; Dass, S.; Satsangi, V. Iron Doped Nanostructured TiO_2 for Photoelectrochemical Generation of Hydrogen. *Int. J. Hydrogen Energy* **2008**, *33*, 5363−5368.
(16) Salvador, P. The Influence of Niobium Doping on the Efficiency of N-TiO_2 Electrode in Water Photoelectrolysis. *Sol. Energy Mater.* **1980**, *2*, 413−421.
(17) Zhou, X.; Liu, N.; Schmuki, P. Photocatalysis with TiO2 Nanotubes: "Colorful" Reactivity and Designing Site-Specific Photocatalytic Centers into TiO_2 Nanotubes. *ACS Catal.* **2017**, *7*, 3210−3235.
(18) Yang, Y.; Zhang, C.; Lai, C.; Zeng, G.; Huang, D.; Cheng, M.; Wang, J.; Chen, F.; Zhou, C.; Xiong, W. BiOX (X = Cl, Br, I) Photocatalytic Nanomaterials: Applications for Fuels and Environmental Management. *Adv. Colloid Interface Sci.* **2018**, *254*, 76−93.
(19) Ye, L.; Su, Y.; Jin, X.; Xie, H.; Zhang, C. Recent Advances in BiOX (X = Cl, Br and I) Photocatalysts: Synthesis, Modification, Facet Effects and Mechanisms. *Environ. Sci.: Nano* **2014**, *1*, 90−112.
(20) Nowotny, M. K.; Sheppard, L. R.; Bak, T.; Nowotny, J. Defect Chemistry of Titanium Dioxide. Application of Defect Engineering in Processing of TiO2-Based Photocatalysts. *J. Phys. Chem. C* **2008**, *112*, 5275−5300.
(21) Ong, S. W. D.; Lin, J.; Seebauer, E. G. Control of Photoactivity over Polycrystalline Anatase TiO_2 Thin Films via Surface Potential. *J. Phys. Chem. C* **2015**, *119*, 27060−27071.
(22) Butler, M. A. Photoelectrolysis and Physical Properties of the Semiconducting Electrode WO_2. *J. Appl. Phys.* **1977**, *48*, 1914−1920.
(23) Schneider, J.; Matsuoka, M.; Takeuchi, M.; Zhang, J.; Horiuchi, Y.; Anpo, M.; Bahnemann, D. W. Understanding TiO_2 Photocatalysis: Mechanisms and Materials. *Chem. Rev.* **2014**, *114*, 9919−9986.
(24) Hagfeldt, A.; Graetzel, M. Light-Induced Redox Reactions in Nanocrystalline Systems. *Chem. Rev.* **1995**, *95*, 49−68.
(25) Smit, G. D. J.; Rogge, S.; Klapwijk, T. M. Scaling of Nano-Schottky-Diodes. *Appl. Phys. Lett.* **2002**, *81*, 3852.
(26) Ohno, T.; Haga, D.; Fujihara, K.; Kaizaki, K.; Matsumura, M. Unique Effects of Iron(III) Ions on Photocatalytic and Photoelectrochemical Properties of Titanium Dioxide. *J. Phys. Chem. B* **1997**, *101*, 6415−6419.
(27) Fujihara, K.; Izumi, S.; Ohno, T.; Matsumura, M. Time-Resolved Photoluminescence of Particulate TiO_2 Photocatalysts Suspended in Aqueous Solutions. *J. Photochem. Photobiol., A* **2000**, *132*, 99−104.
(28) Roy, P.; Kim, D.; Lee, K.; Spiecker, E.; Schmuki, P. TiO_2 Nanotubes and Their Application in Dye-Sensitized Solar Cells. *Nanoscale* **2010**, *2*, 45−59.
(29) Nazeeruddin, M. K.; Kay, A.; Rodicio, I.; Humphry-Baker, R.; Mueller, E.; Liska, P.; Vlachopoulos, N.; Graetzel, M. Conversion of Light to Electricity by Cis-X2Bis (2,2′-Bipyridyl-4,4′-Dicarboxylate) Ruthenium (II) Charge-Transfer Sensitizers (X = Cl−, Br−, I−, CN−, and SCN−) on Nanocrystalline TiO2 Electrodes. *J. Am. Chem. Soc.* **1993**, *115*, 6382−6390.
(30) Hanaor, D. A. H.; Sorrell, C. C. Review of the Anatase to Rutile Phase Transformation. *J. Mater. Sci.* **2011**, *46*, 855−874.
(31) Shannon, R. D.; Pask, J. A. Kinetics of the Anatase-Rutile Transformation. *J. Am. Ceram. Soc.* **1965**, *48*, 391−398.
(32) Bedoya, F.; Allain, J. P.; Dominguez-Gutierrez, F. J.; Krstic, P. S. Effect of Deuterium Irradiation on Graphite Boronized in the NSTX-U Tokamak. *Sci. Rep.* **2019**, *9*, 2435.
(33) Stoller, R. E.; Toloczko, M. B.; Was, G. S.; Certain, A. G.; Dwaraknath, S.; Garner, F. A. On the Use of SRIM for Computing Radiation Damage Exposure. *Nucl. Instrum. Methods Phys. Res., Sect. B* **2013**, *310*, 75−80.
(34) Condon, J. *Surface Area and Porosity Determinations by Physisorption*; Elsevier, 2006.
(35) Klobes, P.; Munro, R. *Porosity and Specific Surface Area Measurements for Solid Materials*. Special Publication (NIST SP); National Institute of Standards and Technology: Gaithersburg, MD, 2006.
(36) Albery, W. J.; O'Shea, G. J.; Smith, A. L. Interpretation and Use of Mott−Schottky Plots at the Semiconductor/Electrolyte Interface. *J. Chem. Soc., Faraday Trans.* **1996**, *92*, 4083−4085.
(37) Enache, C. S.; Schoonman, J.; Krol, R. V. The Photoresponse of Iron- and Carbon-Doped TiO_2 (Anatase) Photoelectrodes. *J. Electroceram.* **2004**, *13*, 177−182.
(38) Dürr, M.; Schmid, A.; Obermaier, M.; Yasuda, A.; Nelles, G. Diffusion Properties of Dye Molecules in Nanoporous TiO_2 Networks. *J. Phys. Chem. A* **2005**, *109*, 3967−3970.
(39) Matos, J.; Ocares-Riquelme, J.; Poon, P. S.; Montaña, R.; García, X.; Campos, K.; Hernández-Garrido, J. C.; Titirici, M. M. C-Doped Anatase TiO2: Adsorption Kinetics and Photocatalytic Degradation of Methylene Blue and Phenol, and Correlations with DFT Estimations. *J. Colloid Interface Sci.* **2019**, *547*, 14−29.
(40) Zhang, T.; Oyama, T.; Aoshima, A.; Hidaka, H.; Zhao, J.; Serpone, N. Photooxidative N-Demethylation of Methylene Blue in Aqueous TiO_2 Dispersions under UV Irradiation. *J. Photochem. Photobiol., A* **2001**, *140*, 163−172.
(41) Houas, A.; Lachheb, H.; Ksibi, M.; Elaloui, E.; Guillard, C.; Herrmann, J.-M. Photocatalytic Degradation Pathway of Methylene Blue in Water. *Appl. Catal., B* **2001**, *31*, 145−157.
(42) Kapinus, E. I.; Viktorova, T. I. Kinetics of the Photocatalytic Degradation of Methylene Blue on Titanium Dioxide. *Theor. Exp. Chem.* **2010**, *46*, 163−167.
(43) Epling, G. A.; Lin, C. Photoassisted Bleaching of Dyes Utilizing TiO_2 and Visible Light. *Chemosphere* **2002**, *46*, 561−570.
(44) Mills, A.; Wang, J. Photobleaching of Methylene Blue Sensitised by TiO_2: An Ambiguous System? *J. Photochem. Photobiol., A* **1999**, *127*, 123.
(45) Wang, G.; Wang, H.; Ling, Y.; Tang, Y.; Yang, X.; Fitzmorris, R. C.; Wang, C.; Zhang, J. Z.; Li, Y. Hydrogen-Treated TiO_2 Nanowire Arrays for Photoelectrochemical Water Splitting. *Nano Lett.* **2011**, *11*, 3026−3033.

https://doi.org/10.1021/acs.jpcc.1c09020
J. Phys. Chem. C 2022, 126, 1376−1388

(46) Chen, X.; Liu, L.; Yu, P. Y.; Mao, S. S. Increasing Solar Absorption for Photocatalysis with Black Hydrogenated Titanium Dioxide Nanocrystals. *Science* **2011**, *331*, 746−750.
(47) Bockris, J. O. M.; Reddy, A. K. N.; Gamboa-Aldeco, M. E. *Modern Electrochemistry 2A*; Kluwer Academic Publishers: Boston, 2002.
(48) Dillon, E. P.; Crouse, C. A.; Barron, A. R. Synthesis, Characterization, and Carbon Dioxide Adsorption of Covalently Attached Polyethyleneimine-Functionalized Single-Wall Carbon Nanotubes. *ACS Nano* **2008**, *2*, 156−164.
(49) Gogotsi, Y. G.; Uvarova, I. v. *Nanostructured Materials and Coatings for Biomedical and Sensor Applications*; Gogotsi, Y. G., Uvarova, I. V., Eds.; Springer Netherlands: Dordrecht, 2003.
(50) Yang, C.-M.; Kanoh, H.; Kaneko, K.; Yudasaka, M.; Iijima, S. Adsorption Behaviors of HiPco Single-Walled Carbon Nanotube Aggregates for Alcohol Vapors. *J. Phys. Chem. B* **2002**, *106*, 8994−8999.
(51) Sham, T. K.; Lazarus, M. S. X-Ray Photoelectron Spectroscopy (XPS) Studies of Clean and Hydrated TiO_2 (Rutile) Surfaces. *Chem. Phys. Lett.* **1979**, *68*, 426−432.
(52) Wang, L.-Q.; Baer, D. R.; Engelhard, M. H.; Shultz, A. N. The Adsorption of Liquid and Vapor Water on TiO_2(110) Surfaces: The Role of Defects. *Surf. Sci.* **1995**, *344*, 237−250.
(53) Erdem, B.; Hunsicker, R. A.; Simmons, G. W.; Sudol, E. D.; Dimonie, V. L.; El-Aasser, M. S. XPS and FTIR Surface Characterization of TiO_2 Particles Used in Polymer Encapsulation. *Langmuir* **2001**, *17*, 2664−2669.
(54) Jensen, H.; Soloviev, A.; Li, Z.; Søgaard, E. G. XPS and FTIR Investigation of the Surface Properties of Different Prepared Titania Nano-Powders. *Appl. Surf. Sci.* **2005**, *246*, 239−249.
(55) Sanjinés, R.; Tang, H.; Berger, H.; Gozzo, F.; Margaritondo, G.; Lévy, F. Electronic Structure of Anatase TiO_2 Oxide. *J. Appl. Phys.* **1994**, *75*, 2945−2951.
(56) Jobin, M.; Taborelli, M.; Descouts, P. Structural Characterization of Oxidized Titanium Surfaces. *J. Appl. Phys.* **1995**, *77*, 5149−5155.
(57) Cai, K.; Müller, M.; Bossert, J.; Rechtenbach, A.; Jandt, K. D. Surface Structure and Composition of Flat Titanium Thin Films as a Function of Film Thickness and Evaporation Rate. *Appl. Surf. Sci.* **2005**, *250*, 252−267.
(58) Sang, L.; Zhang, Y.; Wang, J.; Zhao, Y.; Chen, Y.-t. Correlation of the Depletion Layer with the Helmholtz Layer in the Anatase TiO_2-H_2O Interface: Via Molecular Dynamics Simulations. *Phys. Chem. Chem. Phys.* **2016**, *18*, 15427−15435.
(59) Ozawa, K.; Emori, M.; Yamamoto, S.; Yukawa, R.; Yamamoto, S.; Hobara, R.; Fujikawa, K.; Sakama, H.; Matsuda, I. Electron-Hole Recombination Time at TiO_2 Single-Crystal Surfaces: Influence of Surface Band Bending. *J. Phys. Chem. Lett.* **2014**, *5*, 1953−1957.
(60) Lavrov, E. V. Hydrogen Donor in Anatase TiO_2. *Phys. Rev. B* **2016**, *93*, 045204.
(61) Lavrov, E. V.; Chaplygin, I.; Herklotz, F.; Melnikov, V. V. Hydrogen Donors in Anatase TiO_2. *Phys. Status Solidi B* **2021**, *258*, 2100171.
(62) Murugesan, T.; Perumalsamy, M. Densities and Viscosities of Polyethylene Glycol 2000 + Salt + Water Systems from (298.15 to 318.15) K. *J. Chem. Eng. Data* **2005**, *50*, 1290−1293.
(63) Li, X. Z.; Li, F. B. Study of Au/Au^{3+}-TiO_2 Photocatalysts toward Visible Photooxidation for Water and Wastewater Treatment. *Environ. Sci. Technol.* **2001**, *35*, 2381−2387.
(64) Lindgren, T.; Mwabora, J. M.; Avendaño, E.; Jonsson, J.; Hoel, A.; Granqvist, C.-G.; Lindquist, S.-E. Photoelectrochemical and Optical Properties of Nitrogen Doped Titanium Dioxide Films Prepared by Reactive DC Magnetron Sputtering. *J. Phys. Chem. B* **2003**, *107*, 5709−5716.
(65) Cong, Y.; Zhang, J.; Chen, F.; Anpo, M. Synthesis and Characterization of Nitrogen-Doped TiO_2 Nanophotocatalyst with High Visible Light Activity. *J. Phys. Chem. C* **2007**, *111*, 6976−6982.
(66) Pelaez, M.; Nolan, N. T.; Pillai, S. C.; Seery, M. K.; Falaras, P.; Kontos, A. G.; Dunlop, P. S. M.; Hamilton, J. W. J.; Byrne, J. A.; O'Shea, K.; et al. Review on the Visible Light Active Titanium Dioxide Photocatalysts for Environmental Applications. *Appl. Catal., B* **2012**, *125*, 331−349.
(67) Hurum, D. C.; Agrios, A. G.; Gray, K. A.; Rajh, T.; Thurnauer, M. C. Explaining the Enhanced Photocatalytic Activity of Degussa P25 Mixed-Phase TiO_2 Using EPR. *J. Phys. Chem. B* **2003**, *107*, 4545−4549.
(68) Ni, M.; Leung, M. K. H.; Leung, D. Y. C.; Sumathy, K. A Review and Recent Developments in Photocatalytic Water-Splitting Using TiO_2 for Hydrogen Production. *Renewable Sustainable Energy Rev.* **2007**, *11*, 401−425.
(69) Mukherjee, D.; Barghi, S.; Ray, A. Preparation and Characterization of the TiO_2 Immobilized Polymeric Photocatalyst for Degradation of Aspirin under UV and Solar Light. *Processes* **2013**, *2*, 12−23.
(70) Scanlon, D. O.; Dunnill, C. W.; Buckeridge, J.; Shevlin, S. A.; Logsdail, A. J.; Woodley, S. M.; Catlow, C. R. A.; Powell, M. J.; Palgrave, R. G.; Parkin, I. P.; et al. Band Alignment of Rutile and Anatase TiO_2. *Nat. Mater.* **2013**, *12*, 798−801.
(71) Hashimoto, K.; Irie, H.; Fujishima, A. TiO_2 Photocatalysis: A Historical Overview and Future Prospects. *Jpn. J. Appl. Phys.* **2005**, *44*, 8269−8285.
(72) Yang, L.; Luo, S.; Li, Y.; Xiao, Y.; Kang, Q.; Cai, Q. High Efficient Photocatalytic Degradation of P-Nitrophenol on a Unique Cu_2O/TiO_2 p-n Heterojunction Network Catalyst. *Environ. Sci. Technol.* **2010**, *44*, 7641−7646.
(73) Zhao, Y.; Hou, T.; Li, Y.; Chan, K. S.; Lee, S.-T. Effective Increasing of Optical Absorption of TiO_2 by Introducing Trivalent Titanium. *Appl. Phys. Lett.* **2013**, *102*, 171902.
(74) Mehta, M.; Kodan, N.; Kumar, S.; Kaushal, A.; Mayrhofer, L.; Walter, M.; Moseler, M.; Dey, A.; Krishnamurthy, S.; Basu, S.; et al. Hydrogen Treated Anatase TiO_2: A New Experimental Approach and Further Insights from Theory. *J. Mater. Chem. A* **2016**, *4*, 2670−2681.
(75) Wang, Z.; Yang, C.; Lin, T.; Yin, H.; Chen, P.; Wan, D.; Xu, F.; Huang, F.; Lin, J.; Xie, X.; et al. H-Doped Black Titania with Very High Solar Absorption and Excellent Photocatalysis Enhanced by Localized Surface Plasmon Resonance. *Adv. Funct. Mater.* **2013**, *23*, 5444−5450.
(76) Martha, S.; Chandra Sahoo, P.; Parida, K. M. An Overview on Visible Light Responsive Metal Oxide Based Photocatalysts for Hydrogen Energy Production. *RSC Adv.* **2015**, *5*, 61535−61553.
(77) Kumaravel, V.; Mathew, S.; Bartlett, J.; Pillai, S. C. Photocatalytic Hydrogen Production Using Metal Doped TiO_2: A Review of Recent Advances. *Appl. Catal., B* **2019**, *244*, 1021−1064.
(78) Vijayalakshmi, S. P.; Madras, G. Photocatalytic Degradation of Poly(Ethylene Oxide) and Polyacrylamide. *J. Appl. Polym. Sci.* **2006**, *100*, 3997−4003.
(79) Simangoye Ngobissi, D. E.; Soufi, J.; Vanoye, L.; Richard, D. Photocatalytic Degradation of Hexaethylene Glycol. *Catal. Lett.* **2017**, *147*, 1608−1614.
(80) Henderson, M. A. Surface Science Perspective on TiO_2 Photocatalysis. *Surf. Sci. Rep.* **2011**, *66*, 185−297.
(81) Islam, M. M.; Calatayud, M.; Pacchioni, G. Hydrogen Adsorption and Diffusion on the Anatase TiO_2(101) Surface: A First-Principles Investigation. *J. Phys. Chem. C* **2011**, *115*, 6809−6814.
(82) Bromiley, G. D.; Shiryaev, A. A. Neutron Irradiation and Post-Irradiation Annealing of Rutile (TiO_{2-x}): Effect on Hydrogen Incorporation and Optical Absorption. *Phys. Chem. Miner.* **2006**, *33*, 426−434.
(83) Leshuk, T.; Parviz, R.; Everett, P.; Krishnakumar, H.; Varin, R. A.; Gu, F. Photocatalytic Activity of Hydrogenated TiO_2. *ACS Appl. Mater. Interfaces* **2013**, *5*, 1892−1895.
(84) Nandasiri, M. I.; Shutthanandan, V.; Manandhar, S.; Schwarz, A. M.; Oxenford, L.; Kennedy, J. V.; Thevuthasan, S.; Henderson, M. A. Instability of Hydrogenated TiO_2. *J. Phys. Chem. Lett.* **2015**, *6*, 4627−4632.
(85) Liu, N.; Schneider, C.; Freitag, D.; Zolnhofer, E. M.; Meyer, K.; Schmuki, P. Noble-Metal-Free Photocatalytic H2 Generation: Active

https://doi.org/10.1021/acs.jpcc.1c09020
J. Phys. Chem. C 2022, 126, 1376−1388

and Inactive 'Black' TiO_2 Nanotubes and Synergistic Effects. *Chem.—Eur. J.* **2016**, *22*, 13810−13814.
(86) Rajaraman, T. S.; Parikh, S. P.; Gandhi, V. G. Black TiO_2: A Review of Its Properties and Conflicting Trends. *Chem. Eng. J.* **2020**, *389*, 123918.
(87) Balog, Á.; Samu, G. F.; Pető, S.; Janáky, C. The Mystery of Black TiO_2: Insights from Combined Surface Science and In Situ Electrochemical Methods. *ACS Mater. Au* **2021**, *1*, 157−168.
(88) Wang, S.; Pan, L.; Song, J.-J.; Mi, W.; Zou, J.-J.; Wang, L.; Zhang, X. Titanium-Defected Undoped Anatase TiO_2 with p-Type Conductivity, Room-Temperature Ferromagnetism, and Remarkable Photocatalytic Performance. *J. Am. Chem. Soc.* **2015**, *137*, 2975−2983.
(89) Zhou, W.; Umezawa, N. Viable Approach toward Efficient P-Type Conductivity in Al-Doped Anatase TiO_2 via Strain Engineering. *RSC Adv.* **2017**, *7*, 20542−20547.
(90) Chen, X.; Burda, C. The Electronic Origin of the Visible-Light Absorption Properties of C-, N- and S-Doped TiO_2 Nanomaterials. *J. Am. Chem. Soc.* **2008**, *130*, 5018−5019.
(91) Yu, J. C.; Yu; Ho; Jiang; Zhang. Effects of F- Doping on the Photocatalytic Activity and Microstructures of Nanocrystalline TiO_2 Powders. *Chem. Mater.* **2002**, *14*, 3808−3816.
(92) Zhao, T.; Yanagi, R.; Xu, Y.; He, Y.; Song, Y.; Yang, M.; Hu, S. A Coating Strategy to Achieve Effective Local Charge Separation for Photocatalytic Coevolution. *Proc. Natl. Acad. Sci. U.S.A.* **2021**, *118*, No. e2023552118.

https://doi.org/10.1021/acs.jpcc.1c09020
J. Phys. Chem. C 2022, 126, 1376−1388